Charge Dynamics in Organic Photovoltaic Materials: Interplay between Quantum Diffusion and Quantum Relaxation

Myeong H. Lee,* Juan Aragó, and Alessandro Troisi

Department of Chemistry and Centre of Scientific Computing, University of Warwick, Coventry CV4 7AL, UK

E-mail: myeong.lee@warwick.ac.uk

*To whom correspondence should be addressed

Abstract

This paper discusses the mechanism of generation of free charges in organic photovoltaic cells (OPV) from electrostatically bound electron-hole pairs. The efficiency of this process is explained when interfacial charge-transfer (CT) states are generated by direct optical excitation. We used semiclassical quantum dynamics at short timescale ($\sim$100 fs) and Redfield theory at relatively long timescale ($\sim$10-100 ps) to cover both the process of dissociation and the relaxation to the lowest energy state. Our calculations suggest that a CT state with an intermediate electron-hole separation can evolve into a charge-separated (CS) state on ultrafast timescales ($\sim$100 fs) as a result of quantum diffusion. On long timescales, however, the CS states ultimately relax to the low-energy CT states due to the interaction with the thermal bath, indicating that the yield of free charge carrier generation is determined by the interplay between ultrafast charge separation, due to quantum diffusion, and the much slower quantum relaxation process.

Keywords: Charge separation, Organic photovoltaics, Ehrenfest dynamics, Redfield theory

1 Introduction

Light absorption in donor/acceptor (D/A) heterojunction organic photovoltaic (OPV) materials leads to the formation of spatially localized electron-hole pairs (Frenkel excitons) rather than creating free charge carriers as in inorganic PV materials.[1–3] Photocurrent generation in OPV devices, therefore, requires first the dissociation of Coulombically bound Frenkel excitons into interfacial charge transfer (CT) state excitons (D^+A^-) and then the separation of electron-hole pairs into free electron and hole carriers ($D^+ + A^-$). Because of the low dielectric constant, the binding energy of CT excitons in organic materials is typically an order of magnitude larger than the thermal energy. However, experimental evidences indicate unequivocally that the charge generation process occurs on ultrafast timescale within a few hundred femtoseconds in OPV cells.[4–8] Understanding how the tightly bound electron-hole pair overcomes the Coulomb barrier and dissociates into free charge carriers is therefore one of the long-standing questions in OPV and is crucial for the design of new devices with improved efficiency.

Recent experiments using time-resolved two-photon photoemission (TR-2PPE) spectroscopy and transient absorption spectroscopy suggest that efficient CS is assisted by the *hot* charge-transfer (CT) state with excess photon energy.[4,6,9] However, other experimental evidences indicate that the internal quantum efficiency is independent of whether or not initially generated excited states have higher energy than the thermally relaxed CT states.[10,11] Therefore, the relevant question about what drives ultrafast CS in OPV cells is still open.[12]

A good number of theoretical studies have been performed to provide a quantitative description of the ultrafast CS in OPV cells.[13–22] For example, Tamura and Burghardt[13] attributed fast CS to the two main factors, (i) electron delocalization within the fullerene condensate and (ii) the role of vibronically hot CT states, by carrying out a combined approach of electronic structure calculations and quantum dynamical analysis. Sun and Stafström[14] showed, using nonadiabatic Ehrenfest dynamics, that intermolecular interactions strong enough to delocalize the wavefunctions on the acceptor side are crucial to overcome the Coulomb at-

traction. Similar conclusions have been obtained with a very elementary treatment of the electron-phonon coupling in Ref. 23. Smith and Chin[15] suggested that delocalized electronic eigenstates of the acceptor crystallite can account for both ultrafast CS that occurs on short timescales after exciton dissociation and the separation of the relaxed CT state formed on long timescales before nongeminate recombination takes place. Vázquez and Troisi[16] suggested that Frenkel excitons on donor material dissociate into partially charge-separated states, i.e., *hot* CT states in nature, which can explain efficient charge generation in OPV materials. All of these studies describe the formation of delocalized, higher energy CT states from the Frenkel excitonic states, which are easily transformed into free charges without energy penalty. In other words, it is the resonant coupling of photogenerated singlet excitons to a high-energy manifold of fullerene electronic states that enables efficient charge generation, bypassing localized CT states.

However, it was recently shown experimentally[11] that CS can occur very efficiently via an optically generated CT state. The theoretical studies so far, identifying a CS mechanism via the direct formation of higher energy and more delocalized CT states, are therefore unable to explain this new evidence. In Ref. 11, the lowest energy emissive interfacial CT state was directly and *exclusively* generated from the ground state via optical excitation and the internal quantum efficiency (IQE, or the fraction of photons transformed into charges that are collected at the electrodes) was essentially similar to the IQE measured for incident radiation populating the exciton on the donor material. Direct photoexcitation of the thermally relaxed CT states has been previously carried out by other experimental groups,[10,24,25] and the conclusion was, similarly, that the CT states with excess energy are not required for the free charge carrier generation.

Herein we consider a scenario where the CT states are generated by direct optical excitation with an intermediate electron-hole separation and energy lower than the energy of free charges. Recently, Barker *et al.*[26] showed that such CT states with the intermediate-range electron-hole separation exist by measuring distance distributions of photogenerated charge

pairs for the wide range of OPV blends. They estimated that electron-hole separation in the range of 3-4 nm is critical for the CT states to yield free charge carriers, depending on the tunneling attenuation factor β. The possibility of generating charges in a range of distances near the interface is easily explained by theoretical modeling.[27] CT states with a small hole-electron separation have larger oscillator strength but smaller density, while CT states at intermediate hole-electron separation are more easily formed because their higher density more than compensates for their weaker oscillator strengths.

In this work we aim at finding out whether CT states at intermediate hole-electron separation can still separate into free holes and electrons as a result of quantum diffusion in the short timescale ($\sim$100 fs). Even if charges can be separated on short timescales, the relaxation process of the CS states to low-lying CT states is expected to take place at relatively long timescales ($\sim$10-100 ps). The same relaxation mechanism can be thought to play a role when free hole and electron are trapped in a CT state, which can be considered as an intermediate state for nongeminate charge recombination.

To obtain a complete description of charge dynamics it is therefore important to model the charge dynamics of *both* processes, "low-energy CT to CS states" and "CS to low-energy CT states", which would occur on two different timescales. To this end, we build a model Hamiltonian of the D/A interface and employ two different quantum dynamics methods (Ehrenfest dynamics and Redfield theory) that are expected to properly describe charge dynamics for each regime. We suggest that the competition between the ultrafast charge separation and comparatively slower relaxation determines ultimately the yield of free charge carrier generation.

2 Methods

2.1 Purely electronic dynamics

To build a model Hamiltonian we treat the acceptor crystal as a finite one-dimensional lattice, where each acceptor molecule occupies each lattice point, while a hole on the donor molecule is treated as a point charge fixed in space (see Figure 1). Similar type of model Hamiltonians has been widely used to describe Frenkel exciton dissociation and charge dynamics in D/A heterojunctions.[7,14–17,22,23,27,28] By considering a single electronic state per acceptor site and only the nearest-neighbor interaction between these electronic states the electronic Hamiltonian can be written as

$$\hat{H}^{\mathrm{el}} = \sum_{i=1}^{N} \left[\varepsilon_i |i\rangle\langle i| + \sum_{j=i\pm1} \tau |i\rangle\langle j| \right], \tag{1}$$

where $|i\rangle$ is an electronic state localized on molecule (site) i; N is the total number of sites; L is the distance between adjacent sites (this is also assumed to be the distance between the hole and electron nearest to the interface); $\varepsilon_i = -\frac{e^2}{4\pi\epsilon L i}$ is the on-site energy determined by Coulomb interaction of an electron with a hole separated by distance $L \times i$ in a dielectric medium with a dielectric constant ϵ/ϵ_0; and τ is the electronic coupling between adjacent states that is assumed to be the same for all adjacent pairs.

Realistic charge dynamics is influenced by the electron-phonon coupling at short time and the coupling with the thermal bath at longer time, as discussed in the following sections. Nevertheless, it is also useful to consider the charge dynamics within the simplified Hamiltonian presented above to determine the features of quantum diffusion in the absence of coupling with other degrees of freedom. Charge dynamics governed by Eq. 1 can be described in two different ways. One is to obtain the time evolution of the wavefunction $|\psi(t)\rangle = \sum_i C_i(t)|i\rangle$ by solving the time-dependent Schrödinger equation $i\hbar\frac{\partial}{\partial t}|\psi(t)\rangle = \hat{H}^{\mathrm{el}}|\psi(t)\rangle$ and the other is to obtain time-evolution of the density matrix $\hat{\rho}(t)$ by solving the quantum Liouville equation

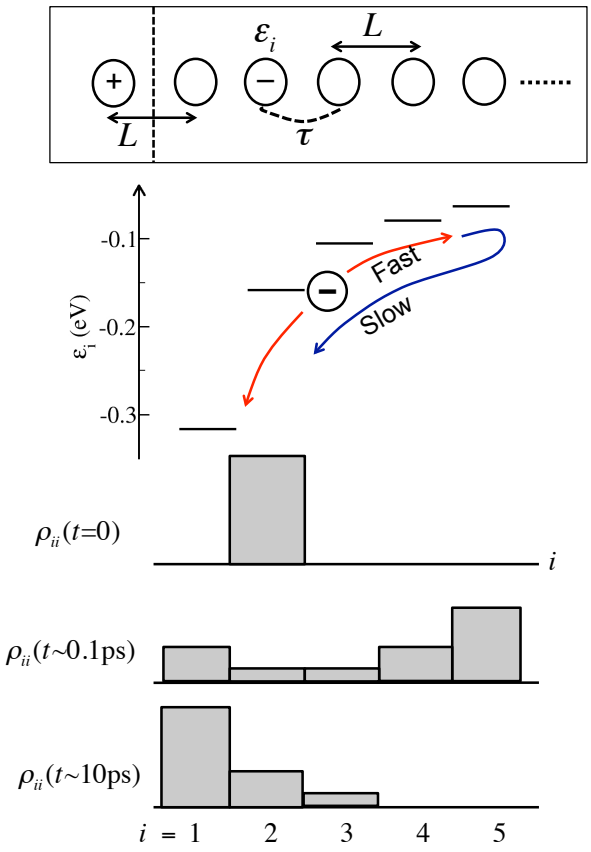

Figure 1: *Top panel*: Schematic of a one-dimensional acceptor lattice model. *Central panel*: corresponding on-site energy ε_i (L=13 Å and ϵ/ϵ_0=3.5). The arrows indicate the short time quantum diffusion and the long time relaxation toward the lowest energy site. *Bottom panel*: Schematics of the time evolution of charge density along the acceptor sites.

$\frac{\partial}{\partial t}\hat{\rho}(t) = -\frac{i}{\hbar}[\hat{H}^{\rm el}, \hat{\rho}(t)]$. Population of charges on each site can be obtained by computing $|C_i(t)|^2$ and $\rho_{ii}(t)$, respectively, which produces identical results in a closed system.

In what follows, we set the electronic Hamiltonian parameters to N=20, L=13 Å, ϵ/ϵ_0=3.5, and τ=0.08 eV unless otherwise noted. (L=13 Å is used to model fullerene derivatives as an acceptor molecule.) Permittivity of a dielectric medium ϵ is close to the reported experimental value[29,30] and τ is an intermediate value encountered in computational studies.[7,14,15,23,27,31,32] Charge is initially localized on the second nearest site to the interface ($|\psi(t=0)\rangle = |2\rangle$), which corresponds to the electron-hole separation of 2.6 nm.

2.2 Ehrenfest dynamics

Thermal fluctuation of nuclei from their equilibrium position leads to modulation of the electronic energy levels and their couplings. In the presence of electron-phonon coupling, the total Hamiltonian can be written as

$$\hat{H}^{\mathrm{tot}} = \hat{H}^{\mathrm{el}} + \hat{H}^{\mathrm{el-ph}} + \hat{H}^{\mathrm{ph}}, \tag{2}$$

where

$$\hat{H}^{\mathrm{el-ph}} = \sum_k \sum_{i=1}^{N} \left[\lambda^{(k)} u_i^{(k)} |i\rangle\langle i| + \sum_{j=i\pm1} \alpha^{(k)} (u_i^{(k)} - u_j^{(k)}) |i\rangle\langle j| \right], \tag{3}$$

$$\hat{H}^{\mathrm{ph}} = \sum_k \sum_{i=1}^{N} \left[\frac{1}{2} m^{(k)} (\dot{u}_i^{(k)})^2 + \frac{1}{2} m^{(k)} (\omega^{(k)} u_i^{(k)})^2 \right], \tag{4}$$

and $\hat{H}^{\mathrm{el}}$ is given by Eq. 1. Here, $\{\lambda^{(k)}\}$ and $\{\alpha^{(k)}\}$ are the local (or Holstein) and non-local (or Peierls) electron-phonon coupling constants, respectively, and $\{u_i^{(k)}\}$ is the displacement of an atom on site i of the nuclear mode k. The first and the second term on the right-hand side of Eq. 3 represents the modulation of the on-site energy ε_i due to the displacement of the nuclei from their equilibrium position and the modulation of the intermolecular electronic coupling τ due to the displacement of the adjacent nuclei relative to each other, respectively. Within an Ehrenfest scheme the phonons are treated as classical harmonic oscillators as described in Eq. 4. Then, the equation of motion for the nuclei position can be written as

$$m^{(k)} \ddot{u}_i^{(k)} = -m^{(k)} (\omega^{(k)})^2 u_i^{(k)} - \frac{\partial}{\partial u_i^{(k)}} \langle \psi(t) | (\hat{H}^{\mathrm{el}} + \hat{H}^{\mathrm{el-ph}}) | \psi(t) \rangle. \tag{5}$$

The last term in Eq. 5 represents the effect of electronic Hamiltonian coupled with the phonons on the nuclear degrees of freedom. Here, initial positions, $\{u_i^{(k)}(0)\}$, and velocities, $\{\dot{u}_i^{(k)}(0)\}$, of the nuclei are selected from the Boltzmann distribution at the room temperature. Details of numerical integration are provided in Ref. 33.

Table 1: Parameter values used in the model Hamiltonian unless otherwise noted. Parameter range used to see its effect on charge dynamics is listed in parentheses. ($m^{(2)}$=392 amu, which corresponds to the mass of a perylene-3,4,9,10-tetracarboxylic dianhydride (PTCDA), is used when L=5 Å.)

		Value	Description
$\hat{H}^{\mathrm{el}}$	L (Å)	13 (5)	lattice spacing
	N	20 (10, 30, 50)	number of acceptor sites
	ϵ/ϵ_0	3.5	dielectric constant
	τ (eV)	0.08 (0.04, 0.16)	electronic coupling
$\hat{H}^{\mathrm{el-ph}}$	$m^{(1)}$ (amu)	6	mass of phonon mode (1)
	$\omega^{(1)}$ (cm^{-1})	1500	frequency of phonon mode (1)
	Λ (eV)	(0.01-0.4)	reorganization energy
	λ (eV/Å)	(0.71-4.48)	local electron-phonon coupling
	$m^{(2)}$ (amu)	910 (392)	mass of phonon mode (2)
	$\omega^{(2)}$ (cm^{-1})	50	frequency of phonon mode (2)
	α (eV/Å)	0.34 (0.03-1.36)	non-local electron-phonon coupling
$\hat{H}^{\mathrm{ph}}$	γ^{-1} (fs)	50 (100)	characteristic timescale of phonon spectral density

The model parameters can be obtained by quantum chemistry calculations and classical molecular dynamics simulations for realistic molecular systems. As in this work we are trying to establish the basic physical principles, we will set the parameters to previously determined literature values and study their effect on the results. The Holstein coupling constant λ is associated with the reorganization energy Λ. Employing a single effective high frequency mode (k=1) for λ is proven to be valid for organic chromophores in charge transfer reactions.[34] In this case, $\lambda^{(k)}$ can be written as $\lambda^{(1)} = \omega^{(1)}\sqrt{m^{(1)}\Lambda}$ and $\lambda^{(k)} = 0$ for $k \neq 1$. We set $\omega^{(1)} = 1500$ cm^{-1} and $m^{(1)} = 6$ amu, which corresponds to C-C/C=C stretching normal mode throughout the simulations.[35]

In general, low frequency modes are responsible for modulating the intermolecular electronic coupling.[36] We assume that this modulation can be represented by a single effective low frequency mode $\omega^{(2)}$ on the basis of previous computational work.[35,37] Here, we set $\omega^{(2)} = 50$ cm^{-1}, which was obtained from the spectral density of τ for organic system,[35,38] and $m^{(2)} = 910$ amu, which corresponds to the total mass of phenyl-C_{61}-butyric acid methyl

ester (PCBM). Reference value of $\alpha^{(2)}$ is set to 0.34 eV/Å, which was determined from the relationship $\sigma_\tau = \alpha^{(2)}\sqrt{2k_{\mathrm{B}}T/m^{(2)}(\omega^{(2)})^2}$, where σ_τ is the standard deviation of τ distribution and approximated to $\sigma_\tau \approx \tau/3$[33] for τ=0.08 eV. Table 1 summarizes the parameters used in this work. In the following we investigate the effect of τ, λ, and α on charge dynamics. (We omit the superscripts in $\lambda^{(k)}$ and $\alpha^{(k)}$, since we consider only one effective mode for each type of electron-phonon coupling).

2.3 Reduced density matrix dynamics

Relaxation process is expected to dominate charge dynamics on long timescales due to the interaction with the thermal bath, resulting in the relaxation of the CS states to the lower-lying CT states. A major drawback of Ehrenfest dynamics is that it fails to achieve thermal equilibrium,[39,40] e.g., non-Boltzmann distribution of equilibrium state population, and does not properly account for decoherence.[41–43] Several approaches are being debated in the literature to improve long-time behavior[44–46] and incorporate decoherence effects[41,47] in Ehrenfest dynamics, but they are outside the scope of our analysis.

Alternative way to study the system relaxation process is to employ the density matrix approach where relaxation dynamics is described in terms of the reduced density operator:

$$\hat{\rho} \equiv \mathrm{Tr}_{\mathrm{B}}\{\hat{\rho}^{\mathrm{tot}}\} = \sum_b \langle b|\hat{\rho}^{\mathrm{tot}}|b\rangle, \tag{6}$$

where $\hat{\rho}^{\mathrm{tot}}$ is the density operator of the "system+bath"; $\mathrm{Tr}_{\mathrm{B}}\{\ \}$ represents the partial trace over the bath degrees of freedom; and $\{|b\rangle\}$ denotes the eigenstates of the bath Hamiltonian. We assume that the system-bath coupling is weak and the bath dynamics is much faster than the system dynamics and therefore memory effects in the reduced density dynamics can be ignored (Markov approximation). It should be noted that Markov approximation is not valid at short times (∼fs) when the characteristic timescales of the system is faster than the timescales on which bath correlation function decays. On these timescales, however,

we do not expect any significant relaxation/dephasing to take place. As we will see, the CS process with reasonable system parameters cannot be possibly Markovian while the relaxation process probably satisfies the Markovian limit. The transition between the two regimes is in general complicated and will not be studied in detail in this work. We, however, discuss the possible interpolation between the two regimes in the results section.

In the Markovian limit the equation of motion for the reduced density operator can be described by the Redfield equation:[48–50]

$$\frac{\partial}{\partial t}\rho_{\mu\nu}(t) = -i\omega_{\mu\nu}\rho_{\mu\nu}(t) + \sum_{\mu'\nu'} R_{\mu\nu,\mu'\nu'}\rho_{\mu'\nu'}(t), \tag{7}$$

where μ, ν stand for eigenstates of the system Hamiltonian and $\omega_{\mu\nu} \equiv (E_\mu - E_\nu)/\hbar$, where E_μ, E_ν are the corresponding eigenvalues. The first term on the right-hand side of Eq. 7 describes system dynamics in the absence of dissipation. System relaxation due to the interaction with the thermal bath is described by the second term via the Redfield tensor $R_{\mu\nu,\mu'\nu'}$, which can be expressed in terms of the damping matrix:

$$R_{\mu\nu,\mu'\nu'} \equiv \Gamma_{\nu'\nu,\mu\mu'} + \Gamma^*_{\mu'\mu,\nu\nu'} - \delta_{\nu\nu'}\sum_\kappa \Gamma_{\mu\kappa,\kappa\mu'} - \delta_{\mu\mu'}\sum_\kappa \Gamma^*_{\nu\kappa,\kappa\nu'}, \tag{8}$$

where the damping matrix $\Gamma_{\mu\nu,\mu'\nu'}$ is given by Fourier-Laplace transforms of the coupling correlation function[50] and mainly determined by the bath correlation functions $\mathfrak{C}(t)$.[49,50] For the system-bath interaction that is linear in the displacement of the bath oscillators, $\hat{H}^{\mathrm{el-ph}} = \sum_k \sum_{i=1}^N \lambda_i^{(k)} u_i^{(k)} |i\rangle\langle i|$, the damping matrix can be written as[51,52]

$$\Gamma_{\mu\nu,\mu'\nu'} \equiv \frac{1}{\hbar^2}\sum_{i,j} \langle e_\mu|i\rangle\langle i|e_\nu\rangle\langle e_{\mu'}|j\rangle\langle j|e_{\nu'}\rangle \mathfrak{C}_{ij}[\omega_{\nu'\mu'}], \tag{9}$$

where the $\mathfrak{C}_{ij}[\omega]$ is the Fourier transform of the $\mathfrak{C}_{ij}(t)$, $\mathfrak{C}_{ij}[\omega] \equiv \int_0^\infty dt e^{i\omega t}\mathfrak{C}_{ij}(t)$, and expressed in terms of bath spectral density $J_{ij}(\omega)$. The imaginary parts of $\mathfrak{C}[\omega]$ represent bath-induced shift of the transition frequency and do not lead to relaxation. Therefore, we only consider

the real parts of $\mathfrak{C}[\omega]$ that are relevant to the system relaxation and given by[51]

$$\text{Re } \mathfrak{C}_{ij}[\omega] = \hbar J_{ij}(\omega)[n_{\text{BE}}(\omega) + 1], \tag{10}$$

where $n_{\text{BE}}(\omega) \equiv [e^{\beta\hbar\omega} - 1]^{-1}$ is the Bose-Einstein distribution function. In this work we employ Drude-Lorentz bath spectral density $J(\omega) = 2\Lambda\frac{\omega\gamma}{\omega^2+\gamma^2}$ [53,54] and assume $J_{ij}(\omega) = \delta_{ij}J(\omega)$.[51] Here, the damping constant γ determines the width and peak position of the spectral density (Λ is the reorganization energy as defined in section 2.2). It should be noted that while only a few local phonon modes are selected when employing Ehrenfest dynamics to describe CS dynamics, continuous spectrum of phonon modes, $J(\omega)$, is employed when using Redfield theory and only the local electron-phonon coupling is considered. Once $\rho_{\mu\nu}$ is obtained from Eq. 7, it can be transformed to the site representation by $\hat{\rho}^{\text{site}} = \hat{U}\hat{\rho}\hat{U}^{-1}$, where $\hat{U}$ is the unitary operator that diagonalizes $\hat{H}^{\text{el}}$ via $\hat{U}^{-1}\hat{H}^{\text{el}}\hat{U}$.

Despite the restrictive assumptions described above, Redfield theory has been shown to provide a simple, computationally efficient, and valuable way to study dissipation due to a thermal environment for a variety of problems.[52,55–58] Recently, Kelly *et al.*[59] proposed a method that combines Ehrenfest mean field theory with the reduced density matrix formalism, which is a non-perturbative, non-Markovian, and non-restrictive on the form of the Hamiltonian with a much lower computational cost than mean-field theory. In this work we choose two different approaches, Ehrenfest dynamics in short times and Redfield theory in long times, which are known to be well-suited in each regime.

3 Results and discussion

3.1 Charge dynamics in the absence of electron-phonon coupling

It is instructive to analyze charge dynamics in the absence of electron-phonon coupling. In fact, while the latter has been proven essential for the quantitative description of exciton dis-

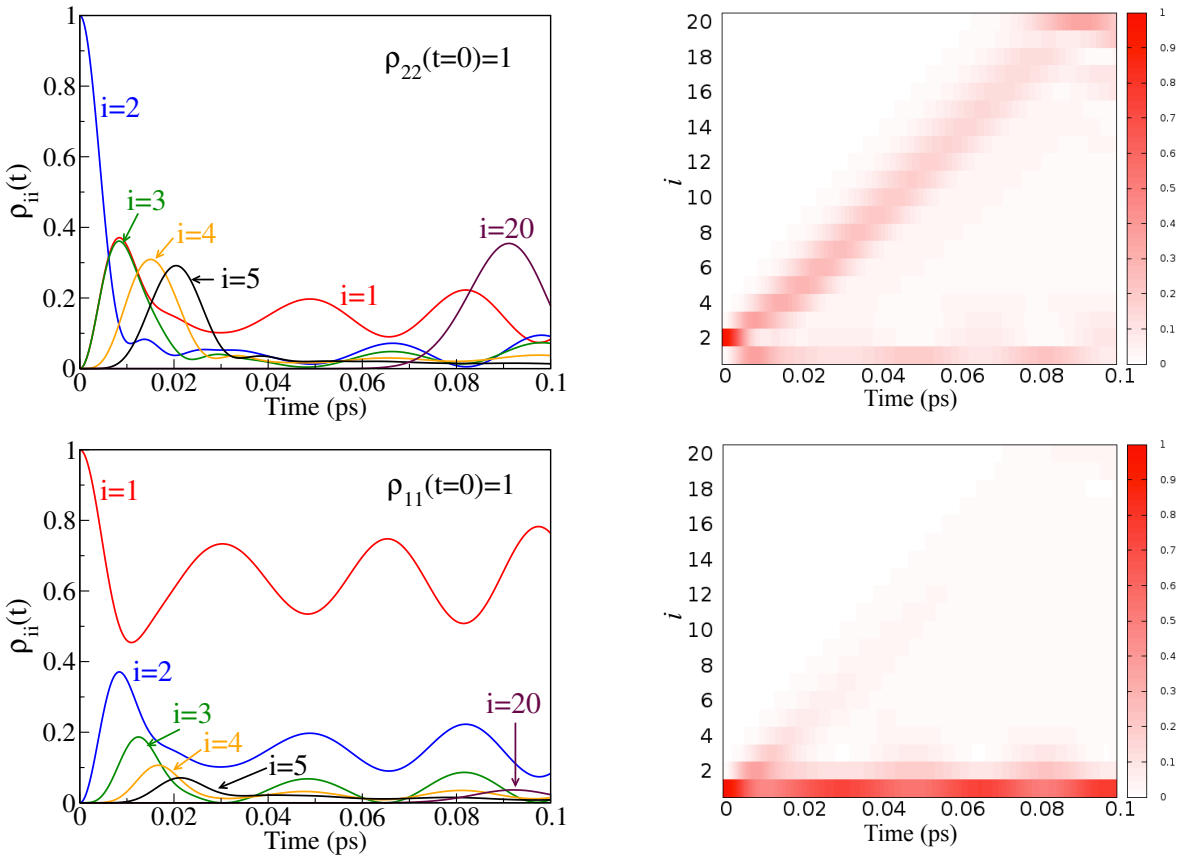

Figure 2: Time evolution of site population in the absence of electron-phonon coupling. On the right panel color-mapped population (white to red when going from ρ_{ii}=0 to ρ_{ii}=1) is plotted where vertical axis denotes a site index. Charge is initially localized on the site i=2 in the upper panel and i=1 in the lower panel, respectively.

sociation,[18,21,60] many qualitative features are present in the simplest possible model without electron-phonon coupling[23] and it is convenient to isolate the phenomenology of a simple, purely electronic Hamiltonian.

Figure 2 (upper panel) shows the time evolution of population $\rho_{ii}(t)$ of several sites (i=1-5, 20) when charge is localized on the site i=2 at t=0. Here, we analyze charge dynamics until the outgoing wavepacket reaches the boundary (set by N=20). Charge propagates with time along the acceptor sites, leaving the D/A interface, and reaches i=20, which corresponds to the electron-hole separation of 26 nm, after 90 fs with population ∼0.35. Note that the population at the lowest energy CT state, ρ_{11}, does not decay to zero. Instead, it fluctuates around 0.1-0.2 with time. This bifurcation behavior of the wavefunction can be more easily seen by plotting the population density map (upper-right panel of Figure 2), where population of each site is color-mapped (red for $\hat{\rho}_{ii}$=1 and white for $\hat{\rho}_{ii}$=0) in the two-dimensional plot (site index on the vertical axis and time on the horizontal axis). It illustrates that the charge population follows two different paths: one propagates outward from the D/A interface and the other is relaxed to the lowest energy CT state. We note in passing that the outgoing wavepacket spreads over a few sites and shows slight increase in the spread as time goes on whereas the charge density relaxed to the lowest energy CT state is more or less localized on i=1.

On the other hand, when the initial state is localized on the lowest energy CT state (i=1), the propagation of the wavefunction away from the interface becomes much weaker. In the lower panel of Figure 2 site population exhibits sign of charge propagation in early times but it fades away with time (ρ_{ii} decreases fast as i increases) while the population at the lowest energy CT state remains high (ρ_{11}=0.5-0.7). Significantly weakened charge propagation behavior is also illustrated by the population density map plotted in the lower-right panel of Figure 2, where the majority of the charge population remains at the lowest energy CT state (i=1) and population at the sites far from the interface is almost negligible. This result indicates that the CS process is not likely to be initiated by a charge located at the shortest possible distance

from the interface but, as long as the initial state possesses an intermediate-range electron-hole separation (e.g., a CT state with 2.6 nm electron-hole separation), the generation of free charge due to quantum diffusion becomes possible. Electron-hole separation of 2.6 nm that is required for efficient CS to occur is close to the lower bound of the critical distance of the charge pairs (3-4 nm) to generate free charges found in Ref. 26.

The expectation value of the energy is constant and below the energy of free charges. However, as the system evolves quantum mechanically, it will have finite probability to be found at higher (or lower) energy sites. In this case, the fast propagation toward higher energy states is facilitated by their higher density. This quantum diffusion process (which as we will see in the next section is slowed down by electron-phonon coupling) cannot take place indefinitely and, at some point, the interaction with the thermal bath will induce dephasing and thermal relaxation toward the lowest energy state as discussed in section 2.3.

Before we proceed to analyze the effect of the electronic Hamiltonian parameters on charge dynamics, we define a few physical quantities for the quantitative analysis of charge dynamics. One simple way to analyze charge dynamics is to obtain the expectation value of the position $\langle x \rangle$ as a function of time. By assuming $\langle i|x|i' \rangle = x_i \delta_{i,i'} = iL\delta_{i,i'}$, $\langle x \rangle$ can be simply obtained by

$$\langle x \rangle = \sum_{i=1}^{N} iL\rho_{ii}(t). \tag{11}$$

However, this definition can give misleading information if the distribution of $\rho_{ii}(t)$ is multimodal, as seen in Figure 2. Therefore, to monitor the propagation of wavepacket leaving the D/A interface, we additionally define the expectation value of the position of the outgoing wavefunction as follows:

$$\langle x \rangle_{\text{outgoing}} \equiv \frac{\sum_{i \geq i_0} iL\rho_{ii}(t)}{\sum_{i \geq i_0} \rho_{ii}(t)}, \tag{12}$$

where i_0 denotes the site where the charge is initially localized. Note that i_0 is included in the summation of Eq. 12, so that $\langle x \rangle_{\text{outgoing}}$ at t=0 gives the initial charge position. The expectation value of the position provides an estimate of electron-hole pair distance as a

function of time, but it does not provide the information of what fraction of charge is leaving the interface. For instance, a small charge at large distances is equivalent to a large charge at small distances. Therefore, we obtain the fraction of *outgoing* charge η defined as:

$$\eta \equiv \sum_{i>i_0} \rho_{ii}(t), \tag{13}$$

which also provides the probability of the wavefunction to be found in the higher-lying states than the initial state.

Figure 3a shows the $\langle x \rangle_{\text{outgoing}}$ as a function of time for different intermolecular electronic couplings τ. To avoid the boundary reflection during charge propagation, arising from the finite size of acceptor lattice model when τ is large, we increase the number of lattice points to N=50 in this case. As expected, the charge leaves the interface at shorter times as τ increases. For instance, it takes 12 fs to reach the site i=5 when τ=0.16 eV whereas it takes 20 fs when τ=0.08 eV and 70 fs when τ=0.04 eV. When τ is very small (=0.04 eV), the CS process becomes very inefficient. It occurs much more slowly and almost stops after 40 fs. Our result that sufficient intermolecular electronic coupling is necessary for CS to occur is in line with other studies[14,15,32] where the increase of intermolecular interactions leads to more delocalization of the acceptor sites and therefore facilitates CS.

We also analyzed charge dynamics for L=5 Å to model flat acceptor molecules (results not shown). As expected, CS dynamics is similar regardless of L if the charge is initially localized with similar electron-hole separation (e.g. we find similar CS dynamics when charge is localized on the site i=4 for L=5 Å and when localized on i=2 for L=13 Å).

3.2 Charge dynamics on short timescales using Ehrenfest scheme

Now we introduce the electron-phonon coupling in the model Hamiltonian to see its effect on charge dynamics. First, we investigate the effect of local electron-phonon coupling λ on charge dynamics. To this end, we set non-local electron-phonon coupling α to zero

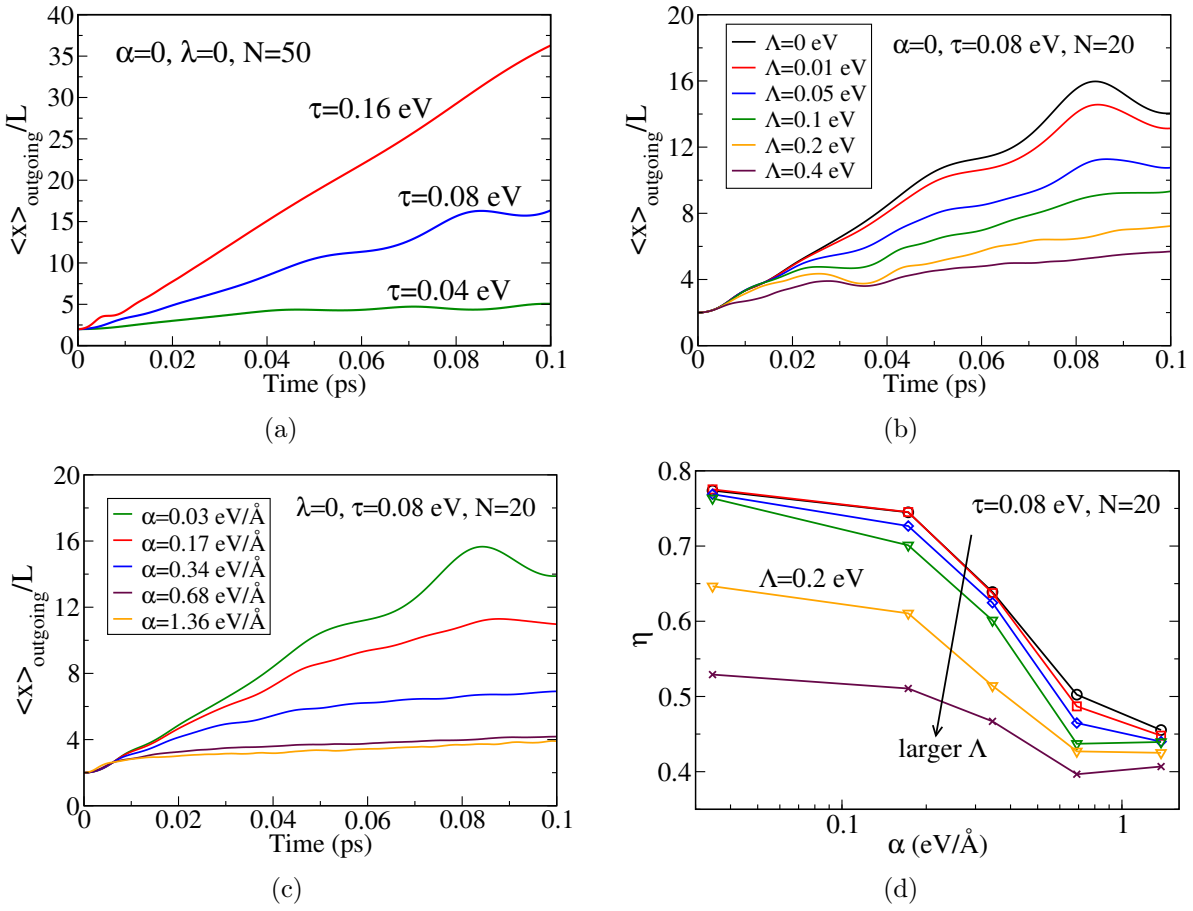

Figure 3: (a) Expectation value of position $\langle x\rangle_{\rm outgoing}/L$ (L=13 Å) for N=50 in the absence of electron-phonon coupling (α=λ=0). (b) $\langle x\rangle_{\rm outgoing}/L$, averaged over 300 trajectories, for different reorganization energies Λ with α=0, τ=0.08 eV and N=20. (c) $\langle x\rangle_{\rm outgoing}/L$, averaged over 300 trajectories, for different non-local electron-phonon coupling constants α with λ=0, τ=0.08 eV and N=20. (d) Fraction of outgoing charge η for different λ and α with τ=0.08 eV and N=20. Each line corresponds to different values of Λ (varying from 0 to 0.4 eV as in (b)).

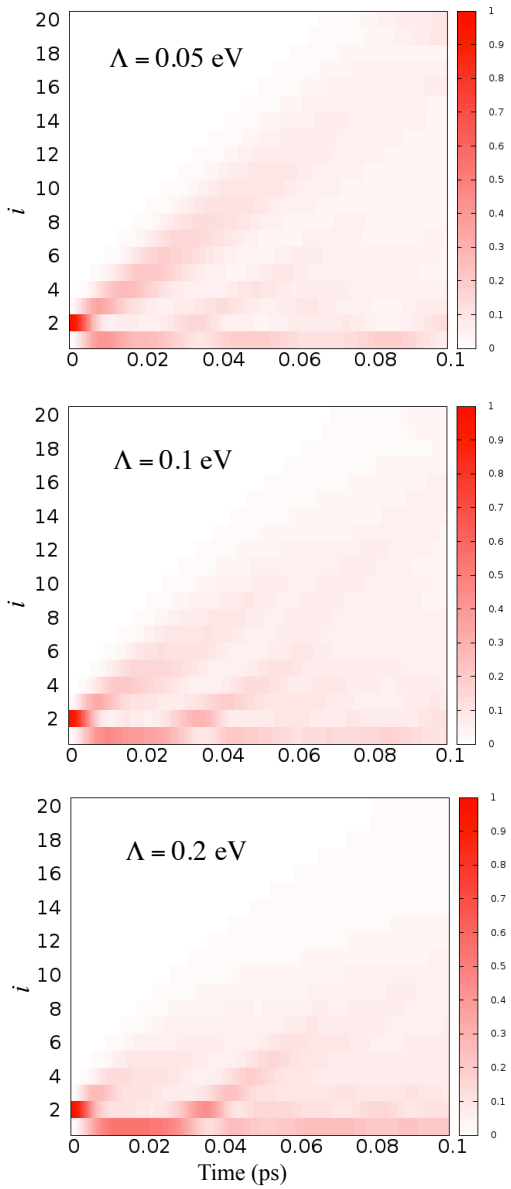

Figure 4: Population density map for Λ=0.05 eV (top), 0.1 eV (middle) and 0.2 eV (bottom). Charge is initially localized on the site i=2 and α is set to zero in all cases.

and vary only reorganization energy Λ, which determines electron-phonon coupling λ by the relationship $\lambda = \omega\sqrt{m\Lambda}$. The charge population density map obtained for different Λ (Figure 4) shows that charge propagation feature becomes weaker as Λ increases and as a result the fraction of charge density at site i=1 (ρ_{11}) increases with Λ. Slowing down of the CS process can be quantitatively analyzed by plotting $\langle x \rangle_{\text{outgoing}}/L$ as shown in Figure 3b. For instance, as Λ increases from 0 to 0.4 eV, $\langle x \rangle_{\text{outgoing}}/L$ at t=85 fs decreases from 16 to 5.4, which corresponds to an electron-hole separation of 21 nm and 7 nm, respectively. Next, we increase α from 0.03 eV/Å to 1.36 eV/Å while keeping λ=0. We find a similar trend of $\langle x \rangle_{\text{outgoing}}/L$ in Figure 3c that the CS process slows down as α increases. Note that as α increases to 0.68 eV/Å or above, CS becomes so slow that increasing α hardly affects charge dynamics any more.

We now vary both λ and α, and plot η at t=80 fs in Figure 3d. Note that η is as high as 0.7-0.8 when both Λ and α remain relatively small. As electron-phonon coupling further increases, η decreases. However, we find $\eta \geq 0.4$ even for the largest electron-phonon coupling constants considered here. Considering the range of reorganization energies (Λ=0.05-0.3 eV)[31,61–64] and the distribution of intermolecular electron-phonon couplings[33,35] in organic semiconducting materials, we can conclude that the CS process can be quite efficient in typical OPV materials. For instance, for the system parameters typical for organic materials (Λ=0.2 eV, α=0.34 eV/Å) we find η=0.51. This represents one of our main results, suggesting that CS can be achieved with a ∼50% probability in the presence of realistic electron-phonon couplings, if the initial CT state can be generated with an intermediate-range electron-hole separation.

3.3 Charge dynamics on long timescales using Redfield equation

We now present charge dynamics on long timescales obtained by Redfield equation. It should be noted that short time dynamics is also correct in this case because the effect of bath is insignificant at very short times. Figure 5a shows the population (diagonal elements of $\hat{\rho}^{\text{site}}$)

for the five sites near the D/A interface using the parameters γ^{-1}=50 fs and Λ=0.05 eV. There are comparatively fewer information on γ and therefore we try a plausible range of γ values as discussed below. We expect that system relaxation occurs much more slowly than the correlation time of the bath fluctuation, γ^{-1}=50 fs, and therefore Markov approximation is valid in this regime. Time evolution of the site population exhibits outgoing charge propagation on short timescales (less than 100 fs), as seen in the previous section using the Ehrenfest method. However, after CS takes place on a short timescale, lower-lying CT states begin to gain population as the quantum relaxation process dominates system dynamics. Site population eventually reaches a plateau after ∼4 ps where ρ_{11} and ρ_{22} are largest and the population of the higher-lying CT states are negligible.

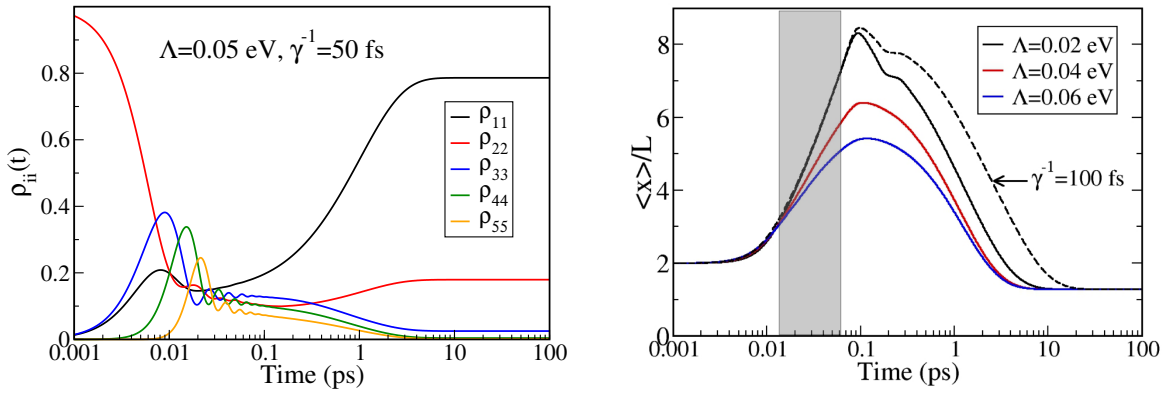

Figure 5: (a) Population of the five sites near the D/A interface. (b) Expectation value of the position $\langle x\rangle/L$ for different values of Λ with γ^{-1}=50 fs. Dashed curve is for γ^{-1}=100 fs and Λ=0.02 eV. Shaded region corresponds to the regime where the charge dynamics cannot be accurately described by the employed quantum dynamics scheme.

Two different processes governing charge dynamics on two different timescales (quantum diffusion on short timescales and quantum relaxation on long timescales) can be easily seen by examining the expectation value of the position. Since we expect charge to relax eventually to the lowest-lying CT states, we evaluate the expectation value of position $\langle x\rangle$ instead of evaluating the position of *outgoing* charge $\langle x\rangle_{\text{outgoing}}$. Figure 5b shows $\langle x\rangle/L$ for different reorganization energies Λ. It starts from $\langle x\rangle/L$=2, where charge is initially populated,

increases until it reaches the largest electron-hole separation on a timescale of ∼100 fs, and then decreases until it reaches an equilibrium value ($\langle x\rangle_{\mathrm{EQ}}/L$=1.3) on a timescale of ∼10 ps.[1] It should be noted that Markov approximation employed here is valid when the timescale of bath correlation function is faster than that of system dynamics. Since the relaxation process will not take effect at very short times, the shaded region in Figure 5b approximately represents the intermediate regime where the quantum dynamics scheme employed in this work may not be valid. We speculate, however, that qualitative picture of charge dynamics in this regime would not significantly deviate from what is described here except for possible variations in CS distances and timescales, based on charge dynamics on long timescales. We note in passing that Ehrenfest dynamics does not reach correct equilibrium as described in section 2.3. For instance, we obtain ρ_{11}=0.1 and $\langle x\rangle/L$ ∼10 at equilibrium.

Figure 5b also shows how parameters Λ and γ affect charge dynamics. As reorganization energy Λ increases, charge propagation occurs more slowly and therefore electron is separated from the hole by shorter distance as seen in the previous section. Timescale on which charge relaxation occurs, on the other hand, is only slightly affected, and the overall behavior of charge dynamics does not critically change with the reorganization energy. We point out that Eq. 7 holds only in the limit of weak system-bath coupling and therefore we keep the value of Λ smaller than τ(=0.08 eV).

Black dashed curve in Figure 5b shows the $\langle x\rangle/L$ for γ^{-1}=100 fs, which is the typical value in photosynthetic excitation energy transfer processes.[51,54,66] When compared with the black solid curve with γ^{-1}=50 fs, system relaxation occurs on slightly longer timescale as the damping constant γ decreases, as expected. On the other hand, charge dynamics on short timescales is hardly affected by γ because the system dynamics in this regime is mostly dominated by the quantum diffusion process rather than quantum relaxation. We found a similar trend of charge dynamics except for a slight increase in the maximal value of $\langle x\rangle$ by 1-2 nm when varying γ^{-1} from 50 fs to 100 fs for larger values of Λ (=0.04 eV and 0.06 eV).

[1] An observation similar to that of Figure 5b was very recently reported by Prof. Xiaoyang Zhu's group on a related system.[65]

Therefore, we conclude that although the distance of separated charge pairs can vary within a few nanometers depending on the system-bath or bath parameters, the overall behavior of charge dynamics does not significantly change and charge relaxation occurs on a timescale of ∼10 ps.

We additionally performed quantum dynamics calculation for different system parameters, such as varying the D-A distance from 9 Å to 19 Å while keeping lattice spacing the same (L=13 Å), increasing the number of sites from N=10 to N=30, and extending the acceptor model from one-dimensional lattice to two-dimensional lattice for different number of sites along the interface. In all cases, we found similar trend of charge dynamics that charges can separate on ultrafast timescale on the order of tens of femtoseconds due to quantum diffusion and they eventually relax to the lowest-energy CT state on a longer timescale on the order of 1-10 ps due to the interaction with the thermal bath.

In our model the only possible fate for the electron carrier is to relax to a bound CT state, from which hole-electron annihilation – and therefore efficiency loss – is the most likely outcome. In a real open system, within the few picosecond of relatively large hole-electron separation, the hole can diffuse away from the interface and the electron can diffuse to a distance where it becomes equilibrated with the quasi-fermi level of the electron acceptor. The picosecond timescale is the one appropriate for device modeling via kinetic Monte Carlo techniques,[67–69] which take into consideration the charge extraction from the electrodes. Conversely, the ultrafast timescale is not suitably described by kinetic methodologies because the charge diffusion takes place coherently for the first hundreds of femtoseconds. Our model accounts for both coherent charge dynamics occurring on a timescale of hundreds of femtoseconds that can be detected by ultrafast spectroscopy measurements and charge relaxation to an equilibrium where standard device modeling techniques (kinetic Monte Carlo, drift-diffusion equations) can be applied to predict microscopic properties of OPV devices. Therefore, the phenomenology described here offers a possible link between the observations in ultrafast pump-probe laser experiments and the electrical measurements of the devices.

Finally, one can note that the methodology used to describe the process of relaxation to a bound CT state from a quasi-CS state can be also used to describe the formation of bound CT state from non-geminate hole-electron pairs.

4 Conclusion

In this paper we modeled charge dynamics in OPV materials for both short (∼fs) and relatively long timescales (∼100 ps) using a simple acceptor lattice model combined with the mixed quantum-classical/quantum dynamics methods in each regime. We have shown that CT states optically generated with intermediate electron-hole distance can separate into CS states (free electrons and holes) on ultrafast timescale without the need for the formation of hot/delocalized CT states, which can explain recent experimental findings that CT states with excess energy are not required for the free charge carrier generation in OPV materials. In the presence of both local and non-local electron-phonon couplings, charge separation is slowed down but still achieved with ∼50 % probability. On long timescales, however, the quantum relaxation process eventually governs charge dynamics and CS states relax to the lowest energy CT states, which can form a bound polaron pair with a hole and undergo non-geminate charge recombination process. Our findings, therefore, suggest that the yield of free charge carrier generation in OPV devices may result from the interplay between the two competing processes: ultrafast charge separation resulting from quantum diffusion and much slower quantum relaxation arising from the interaction with the environment, thereby offering a new insight into the mechanism of free charge carrier generation in OPV materials. We have verified that the results are not qualitatively influenced by the choice of the system parameter. On the other hand, we have noted that a number of simplifications are necessary to achieve a description of the quantum relaxation in the model system. For example, the weak system-bath coupling limit might not be fully valid for OPV materials and, in any case, it is essential to predict the characteristic timescale for quantum relaxation from the

material characteristics rather than phenomenological models. Employing quantum dynamics methods that are less restrictive and material specific appears to be essential to describe accurately the dynamics of charge generation.

Acknowledgement

This work was supported by ERC (Grant No. 615834) and a Marie Curie Intra European Fellowship (FP7-PEOPLE-2012-IEF-329513).

References

1. Kippelen, B.; Brédas, J.-L. Organic Photovoltaics. *Energy Environ. Sci.* **2009**, *2*, 251–261.

2. Benanti, T. L.; Venkataraman, D. Organic Solar Cells: An Overview Focusing on Active Layer Morphology. *Photosynth. Res.* **2006**, *87*, 73–81.

3. Gregg, B. A.; Hanna, M. C. Comparing Organic to Inorganic Photovoltaic Cells: Theory, Experiment, and Simulation. *J. App. Phys.* **2003**, *93*, 3605–3614.

4. Muntwiler, M.; Yang, Q.; Tisdale, W. A.; Zhu, X.-Y. Coulomb Barrier for Charge Separation at an Organic Semiconductor Interface. *Phys. Rev. Lett.* **2008**, *101*, 196403.

5. Grancini, G.; Maiuri, M.; Fazzi, D.; Petrozza, A.; Egelhaaf, H.-J.; Brida, D.; Cerullo, G.; Lanzani, G. Hot Exciton Dissociation in Polymer Solar Cells. *Nature Mater.* **2013**, *12*, 29–33.

6. Jailaubekov, A. E.; Willard, A. P.; Tritsch, J. R.; Chan, W.-L.; Sai, N.; Gearba, R.; Kaake, L. G.; Williams, K. J.; Leung, K.; Rossky, P. J. et al. Hot Charge-Transfer Excitons Set the Time Limit for Charge Separation at Donor/Acceptor Interfaces in Organic Photovoltaics. *Nature Mater.* **2013**, *12*, 66–73.

7. Gélinas, S.; Rao, A.; Kumar, A.; Smith, S. L.; Chin, A. W.; Clark, J.; van der Poll, T. S.; Bazan, G. C.; Friend, R. H. Ultrafast Long-Range Charge Separation in Organic Semiconductor Photovoltaic Diodes. *Science* **2014**, *343*, 512–516.

8. Provencher, F.; Bérubé, N.; Parker, A. W.; Greetham, G. M.; Towrie, M.; Hellmann, C.; Côté, M.; Stingelin, N.; Silva, C.; Hayes, S. C. Direct Observation of Ultrafast Long-Range Charge Separation at Polymer-Fullerene Heterojunctions. *Nature Commun.* **2014**, *5*, 4288.

9. Ohkita, H.; Cook, S.; Astuti, Y.; Duffy, W.; Tierney, S.; Zhang, W.; Heeney, M.; McCulloch, I.; Nelson, J.; Bradley, D. D. C. et al. Charge Carrier Formation in Polythiophene/Fullerene Blend Films Studied by Transient Absorption Spectroscopy. *J. Am. Chem. Soc.* **2008**, *130*, 3030–3042.

10. Lee, J.; Vandewal, K.; Yost, S. R.; Bahlke, M. E.; Goris, L.; Baldo, M. A.; Manca, J. V.; Voorhis, T. V. Charge Transfer State versus Hot Exciton Dissociation in Polymer-Fullerene Blended Solar Cells. *J. Am. Chem. Soc.* **2010**, *132*, 11878–11880.

11. Vandewal, K.; Albrecht, S.; Hoke, E. T.; Graham, K. R.; Widmer, J.; Douglas, J. D.; Schubert, M.; Mateker, W. R.; Bloking, J. T.; Burkhard, G. F. et al. Efficient Charge Generation by Relaxed Charge-Transfer States at Organic Interfaces. *Nature Mater.* **2014**, *13*, 63–68.

12. Gao, F.; Inganäs, O. Charge generation in polymer-fullerene bulk-heterojunction solar cells. *Phys. Chem. Chem. Phys.* **2014**, *16*, 20291–20304.

13. Tamura, H.; Burghardt, I. Ultrafast Charge Separation in Organic Photovoltaics Enhanced by Charge Delocalization and Vibronically Hot Exciton Dissociation. *J. Am. Chem. Soc.* **2013**, *135*, 16364–16367.

14. Sun, Z.; Stafström, S. Dynamics of Charge Separation at an Organic Donor-Acceptor Interface. *Phys. Rev. B* **2014**, *90*, 115420.

15. Smith, S. L.; Chin, A. W. Ultrafast Charge Separation and Nongeminate Electron-Hole Recombination in Organic Photovoltaics. *Phys. Chem. Chem. Phys.* **2014**, *16*, 20305–20309.

16. Vázquez, H.; Troisi, A. Calculation of Rates of Exciton Dissociation into Hot Charge-Transfer States in Model Organic Photovoltaic Interfaces. *Phys. Rev. B* **2013**, *88*, 205304.

17. Caruso, D.; Troisi, A. Long-Range Exciton Dissociation in Organic Solar Cells. *Proc. Natl. Acad. Sci. USA* **2012**, *109*, 13498–13502.

18. Bittner, E. R.; Silva, C. Noise-Induced Quantum Coherence Drives Photo-Carrier Generation Dynamics at Polymeric Semiconductor Heterojunctions. *Nature Commun.* **2014**, *5*, 3119.

19. Duchemin, I.; Blase, X. Resonant Hot Charge-Transfer Excitations in Fullerene-Porpyrin Complexes: Many-Body Bethe-Salpeter Study. *Phys. Rev. B* **2013**, *87*, 245412.

20. Savoie, B. M.; Rao, A.; Bakulin, A. A.; Gelinas, S.; Movaghar, B.; Friend, R. H.; Marks, T. J.; Ratner, M. A. Unequal Partnership: Asymmetric Roles of Polymeric Donor and Fullerene Acceptor in Generating Free Charge. *J. Am. Chem. Soc.* **2014**, *136*, 2876–2884.

21. Han, L.; Zhong, X.; Liang, W.; Zhao, Y. Energy Relaxation and Separation of a Hot Electron-Hole Pair in Organic Aggregates from a Time-Dependent Wavepacket Diffusion Method. *J. Chem. Phys.* **2014**, *140*, 214107.

22. Kocherzhenko, A. A.; Lee, D.; Forsuelo, M. A.; Whaley, K. B. Coherent and Incoherent Contributions to Charge Separation in Multichromophore Systems. *J. Phys. Chem. C* **2015**, *119*, 7590–7603.

23. Troisi, A. How Quasi-Free Holes and Electrons Are Generated in Organic Photovoltaic Interfaces. *Faraday Discuss.* **2013**, *163*, 377–392.

24. van der Hofstad, T. G. J.; Nuzzo, D. D.; van den Berg, M.; Janssen, R. A. J.; Meskers, S. C. J. Influence of Photon Excess Energy on Charge Carrier Dynamics in a Polymer-Fullerene Solar Cell. *Adv. Energy Mater.* **2012**, *2*, 1095–1099.

25. Parkinson, P.; Lloyd-Hughes, J.; Johnston, M. B.; Herz, L. M. Efficient Generation of

Charges via Below-Gap Photoexcitation of Polymer-Fullerene Blend Films Investigated by Terahertz Spectroscopy. *Phys. Rev. B* **2008**, *78*, 115321.

26. Barker, A. J.; Chen, K.; Hodgkiss, J. M. Distance Distributions of Photogenerated Charge Pairs in Organic Photovoltaic Cells. *J. Am. Chem. Soc.* **2014**, *136*, 12018–12026.

27. Ma, H.; Troisi, A. Direct Optical Generation of Long-Range Charge Transfer States in Organic Photovoltaics. *Adv. Mater.* **2014**, *26*, 6163–6167.

28. Sun, Z.; Stafström, S. Dynamics of Exciton Dissociation in Donor-Acceptor Polymer Heterojunctions. *J. Chem. Phys.* **2013**, *138*, 164905.

29. Koster, L. J. A.; Mihailetchi, V. D.; Blom, P. W. M. Ultimate Efficiency of Polymer/Fullerene Bulk Heterojunction Solar Cells. *Appl. Phys. Lett.* **2006**, *88*, 093511.

30. Moulé, A. J.; Meerholz, K. Interference Method for the Determination of the Complex Refractive Index of Thin Polymer Layers. *Appl. Phys. Lett.* **2007**, *91*, 061901.

31. Coropceanu, V.; Cornil, J.; da Silva Filho, D. A.; Olivier, Y.; Silbey, R.; Brédas, J.-L. Charge Transport in Organic Semiconductors. *Chem. Rev.* **2007**, *107*, 926–952.

32. Tamura, H.; Tsukada, M. Role of Intermolecular Charge Delocalization on Electron Transport in Fullerene Aggregates. *Phys. Rev. B* **2012**, *85*, 054301.

33. Troisi, A.; Orlandi, G. Charge-Transport Regime of Crystalline Organic Semiconductors: Diffusion Limit by Thermal Off-Diagonal Electronic Disorder. *Phys. Rev. Lett.* **2006**, *96*, 086601.

34. Jortner, J. Temperature Dependent Activation Energy for Electron Transfer between Biological Molecules. *J. Chem. Phys.* **1976**, *64*, 4860.

35. Troisi, A. Predictions of the Absolute Charge Mobility of Molecular Semiconductors: the Case of Rubrene. *Adv. Mater.* **2007**, *19*, 2000–2004.

36. Troisi, A.; Orlandi, G. Dynamics of the Intermolecular Transfer Integral in Crystalline Organic Semiconductors. *J. Phys. Chem. A* **2006**, *110*, 4065–4070.

37. Troisi, A. Dynamic Disorder in Molecular Semiconductors: Charge Transport in Two Dimensions. *J. Chem. Phys.* **2011**, *134*, 034702.

38. Cheung, D. L.; Troisi, A. Theoretical Study of the Organic Photovoltaic Electron Acceptor PCBM: Morphology, Electronic Structure, and Charge Localization. *J. Phys. Chem. C* **2010**, *114*, 20479–20488.

39. Parandekar, P. V.; Tully, J. C. Mixed Quantum-Classical Equilibrium. *J. Chem. Phys.* **2005**, *122*, 094102.

40. Parandekar, P. V.; Tully, J. C. Detailed Balance in Ehrenfest Mixed Quantum-Classical Dynamics. *J. Chem. Theory Comput.* **2006**, *2*, 229–235.

41. Akimov, A. V.; Long, R.; Prezhdo, O. V. Coherence Penalty Functional: A Simple Method for Adding Decoherence in Ehrenfest Dynamics. *J. Chem. Phys.* **2014**, *140*, 194107.

42. Yonehara, T.; Hanasaki, K.; Takatsuka, K. Fundamental Approaches to Nonadiabaticity: Toward a Chemical Theory beyond the Born-Oppenheimer Paradigm. *Chem. Rev.* **2012**, *112*, 499–542.

43. Käb, G. Statistical Mechanics of Mean Field Ehrenfest Quantum/Classical Molecular Dynamics: The Damped Harmonic Oscillator. *J. Phys. Chem. A* **2004**, *108*, 8866–8877.

44. Bastida, A.; Cruz, C.; Zúñiga, J.; Requena, A.; Miguel, B. A Modified Ehrenfest Method that Achieves Boltzmann Quantum State Populations. *Chem. Phys. Lett.* **2006**, *417*, 53–57.

45. Bastida, A.; Cruz, C.; Zúñiga, J.; Requena, A.; Miguel, B. The Ehrenfest Method with

Quantum Corrections to Simulate the Relaxation of Molecules in Solution: Equilibrium and Dynamics. *J. Chem. Phys.* **2007**, *126*, 014503.

46. Aghtar, M.; Liebers, J.; Strümpfer, J.; Schulten, K. Juxtaposing Density Matrix and Classical Path-Based Wave Packet Dynamics. *J. Chem. Phys.* **2012**, *136*, 214101.

47. Subotnik, J. E. Augmented Ehrenfest Dynamics Yields a Rate for Surface Hopping. *J. Chem. Phys.* **2010**, *132*, 134112.

48. Redfield, A. G. On the Theory of Relaxation Processes. *IBM J. Res. Dev.* **1957**, *1*, 19.

49. May, V.; Kühn, O. *Charge and Energy Transfer Dynamics in Molecular Systems*, 3rd ed.; Willey-VCH: Berlin, 2011.

50. Nitzan, A. *Chemical Dynamics in Condensed Phases*; Oxford University Press: New York, 2006.

51. Ishizaki, A.; Fleming, G. R. On the Adequacy of the Redfield Equation and Related Approaches to the Study of Quantum Dynamics in Electronic Energy Transfer. *J. Chem. Phys.* **2009**, *130*, 234110.

52. Egorova, D.; Thoss, M.; Domcke, W.; Wang, H. Modeling of Ultrafast Electron-Transfer Processes: Validity of Multilevel Redfield Theory. *J. Chem. Phys.* **2003**, *119*, 2761.

53. Mukamel, S. *Principles of Nonlinear Optical Spectroscopy*; Oxford: New York, 1995.

54. Kell, A.; Feng, X.; Reppert, M.; Jankowiak, R. On the Shape of the Phonon Spectral Density in Photosynthetic Complexes. *J. Phys. Chem. B* **2013**, *117*, 7317–7323.

55. Egorova, D.; Gelin, M. F.; Domcke, W. Time- and Frequency-Resolved Fluorescence Spectra of Nonadiabatic Dissipative Systems: What Photons can Tell Us. *J. Chem. Phys.* **2005**, *122*, 134504.

56. Hahn, S.; Stock, G. Ultrafast *Cis-Trans* Photoswitching: A Model Study. *J. Chem. Phys.* **2002**, *116*, 1085.

57. Kühl, A.; Domcke, W. Multilevel Redfield Description of the Dissipative Dynamics at Conical Intersections. *J. Chem. Phys.* **2002**, *116*, 263.

58. Segal, D.; Nitzan, A.; Davis, W. B.; Wasielewsk, M. R.; Ratner, M. A. Electron Transfer Rates in Bridged Molecular Systems 2. A Steady-State Analysis of Coherent Tunneling and Thermal Transitions. *J. Phys. Chem. B* **2000**, *104*, 3817–3829.

59. Kelly, A.; Brackbill, N.; Markland, T. E. Accurate Nonadiabatic Quantum Dynamics on the Cheap: Making the Most of Mean Field Theory with Master Equations. *J. Chem. Phys.* **2015**, *142*, 094110.

60. Falke, S. M.; Rozzi, C. A.; Brida, D.; Maiuri, M.; Amato, M.; Sommer, E.; Sio, A. D.; Rubio, A.; Cerullo, G.; Molinari, E. et al. Coherent Ultrafast Charge Transfer in an Organic Photovoltaic Blend. *Science* **2014**, *344*, 1001–1005.

61. Devos, A.; Lannoo, M. Electron-Phonon Coupling for Aromatic Molecular Crystals: Possible Consequences for Their Superconductivity. *Phys. Rev. B* **1998**, *58*, 8236.

62. Malagoli, M.; Coropceanu, V.; da Silva Filho, D. A.; Brédas, J. L. A Multimode Analysis of the Gas-Phase Photoelectron Spectra in Oligoacenes. *J. Chem. Phys.* **2004**, *120*, 7490.

63. da Silva Filho, D. A.; Kim, E.-G.; Brédas, J.-L. Transport Properties in the Rubrene Crystal: Electronic Coupling and Vibrational Reorganization Energy. *Adv. Mater.* **2005**, *17*, 1072–1076.

64. MacKenzie, R. C. I.; Frost, J. M.; Nelson, J. A Numerical Study of Mobility in Thin Films of Fullerene Derivatives. *J. Chem. Phys.* **2010**, *132*, 064904.

65. Monahan, N. R.; Williams, K. W.; Kumar, B.; Nuckolls, C.; Zhu, X. Y. Direct Observation of Entropy-Driven Electron-hole Pair Separation at an Organic Semiconductor Interface. *Phys. Rev. Lett.* **2015**, in press.

66. Ishizaki, A.; Fleming, G. R. Unified Treatment of Quantum Coherent and Incoherent Hopping Dynamics in Electronic Energy Transfer: Reduced Hierarchy Equation Approach. *J. Chem. Phys.* **2009**, *130*, 234111.

67. Groves, C. Developing Understanding of Organic Photovoltaic Devices: Kinetic Monte Carlo Models of Geminate and Non-Geminate Recombination, Charge Transport and Charge Extraction. *Energy Environ. Sci.* **2013**, *6*, 3202–3217.

68. Melianas, A.; Pranculis, V.; A. Devižis, V. G.; Inganäs, O.; Kemerink, M. Dispersion-Dominated Photocurrent in Polymer:Fullerene Solar Cells. *Adv. Funct. Mater.* **2014**, *24*, 4507–4514.

69. Nelson, J.; Kwiatkowski, J. J.; Kirkpatrick, J.; Frost, J. M. Modeling Charge Transport in Organic Photovoltaic Materials. *Acc. Chem. Res.* **2009**, *42*, 1768–1778.

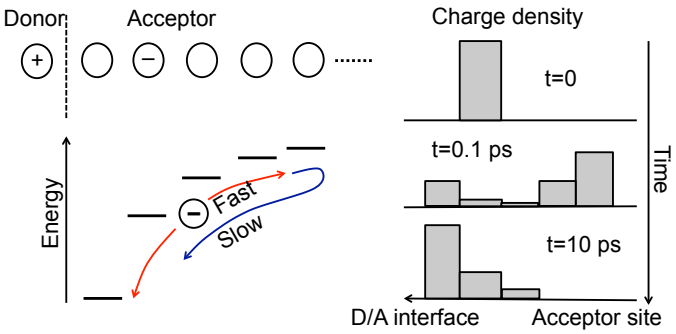

For Table of Contents Only